Gravitationally Lensed Black Hole Emission Tomography
Supplementary Material

Aviad Levis[1*], Pratul P. Srinivasan[2*], Andrew A. Chael[3†], Ren Ng[4], Katherine L. Bouman[1]

[1]California Institute of Technology [2]Google Research [3]Princeton [4]UC Berkeley

Contents

S1. General Relativistic Ray Tracing

In General Relativity, light rays follow curved through four-dimensional space, where space and time are treated on equal footing. For raytracing paths from a camera through the spacetime around a black hole, paths are defined as a "four-vector"[1] x^μ which is a function of a ray distance parameter s. That is,

$$\Gamma = x^\mu(s) \quad , \quad \text{where } \mu \in (t, r, \theta, \phi). \tag{S1}$$

We use spherical polar ("Boyer-Lindquist") coordinates where the index μ runs over the time t, the polar radius r, the polar angle θ and the azimuthal angle ϕ. We use units where we set the speed of light $c = 1$ and Newton's constant $G = 1$, so the radial coordinate r, time coordinate t, ray parameter s, and black hole mass M all have units of distance. Typically, for a black hole of mass M, we measure distance and time in terms of the gravitational length scale:

$$r_{\rm g} = \frac{GM}{c^2} = M \quad (\text{in dimensionless units where } G = c = 1). \tag{S2}$$

In computations, we usually set $M = 1$ and restore units at the end using the length scale $r_{\rm g}$.

We consider black holes which may have non-zero angular momentum. Rotating black holes in General Relativity are described by the Kerr metric: they have two parameters, their mass M and "spin" a. Black holes described by the Kerr metric have an upper limit on their angular momentum set by the mass. In computations when we set the black hole mass $M = 1$, this limit implies that a must be in the range $0 \leq a < 1$.

* Authors contributed equally to this work.

† NASA Hubble Fellowship Program, Einstein Fellow.

[1]In GR notation, Greek indices are used for vectors or tensors with four components in a specific dimension (e.g. the 4-vector x^μ, or 4×4 tensor $T^{\mu\nu}$.)

In general spacetimes, the trajectory $x^\mu(s)$ can be obtained by solving the geodesic equation, which is second order in s [3]. In the Kerr spacetime around a black hole, the differential equation can be reduced to first order [5, 6]:

$$\frac{dx^\mu}{ds} = p^\mu(x), \tag{S3}$$

where p^μ represent the four components of the light ray's momentum. These momentum components depend only on the spatial position x^μ and three constants of motion that are conserved along the entire ray. These constants are the light ray's energy-at-infinity E, the light ray's angular momentum λ, and the "Carter constant" η. Explicitly, the four components of the momentum are [6]:

$$\frac{\Sigma(r,\theta)}{E}\, p^t = \frac{r^2+a^2}{\Delta(r)}\left(r^2+a^2-a\lambda\right) + a\left(\lambda - a\sin^2\theta\right) \tag{S4}$$

$$\frac{\Sigma(r,\theta)}{E}\, p^r = \pm\sqrt{\mathcal{R}(r)} \tag{S5}$$

$$\frac{\Sigma(r,\theta)}{E}\, p^\theta = \pm\sqrt{\Theta(\theta)} \tag{S6}$$

$$\frac{\Sigma(r,\theta)}{E}\, p^\phi = \frac{a}{\Delta(r)}\left(r^2+a^2-a\lambda\right) + \frac{\lambda}{\sin^2\theta} - a. \tag{S7}$$

The $\pm$ signs in the radial component p^r and polar component p^θ determine the direction of the ray. Both components have constant sign until the ray reaches a turning point $p^r = 0$ or $p^\theta = 0$, where the sign of the respective component switches. The ray's path $x^\mu(s)$ is unaffected by the energy E which scales the momentum vector, so we usually set $E = 1$ in computations.

In the photon momentum Eqs. (S4)–(S7), $\Delta(r)$ and $\Sigma(r,\theta)$ are depend only on position:

$$\Delta(r) = r^2 + a^2 - 2r_{\rm g} \tag{S8}$$

$$\Sigma(r,\theta) = r^2 + a^2\cos^2\theta, \tag{S9}$$

and $\mathcal{R}(r)$ and $\Theta(\theta)$ are radial and angular potentials that depend on their respective coordinate and the conserved constants (λ,η):

$$\mathcal{R}(r) = \left(r^2+a^2-a\lambda\right)^2 - \Delta(r)\left[\eta + (\lambda-a)^2\right] \tag{S10}$$

$$\Theta(\theta) = \eta + a^2\cos^2\theta - \lambda^2\cot^2\theta. \tag{S11}$$

Given the differential equation (S3) to compute the trajectory $x^\mu(s)$ in space and time, we only need a prescription to determine the constants of motion (λ, η) along a particular ray trajectory that ends at a pixel on our camera. The camera is situated at a time $t = t_{\rm o}$, radius $r = r_{\rm o}$, polar angle $\theta = \theta_{\rm o}$ and azimuthal angle $\phi = 0$. Remarkably, at large $r_o \to \infty$, the constants of motion (λ,η) for the trajectory that ends up on a pixel are determined entirely by the pixel coordinates (α,β) in a particular coordinate system.

We use coordinates where $(\alpha,\beta) = (0,0)$ marks a straight line to the black hole (i.e. a line of constant $\theta = \theta_o$ and $\phi = 0$). The positive $\beta-$axis is aligned with the direction of the black hole angular momentum vector. The coordinates (α,β) are measured in the same units of distance $r_{\rm g}$ as the radial distance r from the black hole[2]. In this coordinate system, the conserved constants of motion are: [1]

$$\begin{aligned}\lambda &= -\alpha\sin\theta_o \\ \eta &= (\alpha^2-a^2)\cos^2\theta_o + \beta^2.\end{aligned} \tag{S12}$$

In summary, to compute the curved trajectory of a light ray around a black hole that ends on a given pixel of our camera, we first use the pixel coordinates (α,β) to compute the constants (λ,η) using Eq. (S12). Then we use these constants and the position along the ray $x^\mu(s)$ to compute the ray's momentum using Eqs. (S4)–(S7). From the momentum, we can trace the ray forward or backward along its trajectory, parameterized by s, with the differential equation S3. Solving Eq. (S3) can be done numerically, though care must be taken at radial and angular turning points where either p^r or p^θ goes through zero [5, 7]. The integration can also be done explicitly using elliptic integrals [5, 6].

[2] If we are observing the black hole a distance D away, the image at an angular coordinate (α/D,β/D), measured in radians, degrees, or microarcseconds are what we actually measure with a telescope. The characteristic angular size of structure in our image is $r_{\rm g}/D$.

S2. Complex 3D Emission: 3D Digits in Orbit

A key aspect of BH-NeRF is the ability to, in principle, recover arbitrary non-parametric emission distributions. This ability enables novel scientific discovery. We demonstrate this in Fig. S1 by recovering 3D MNIST [4] digits in orbit around a black hole. The digits '0'–'4' are orbiting at a random orientation. Figure S1 shows the ground truth and recovery of $e_0(\mathbf{x})$ for different measurement models (full image, ngEHT, EHT). Different rows show the volumes from different directions, where the observation direction is indicated by the green square. Some features become obscured by the blurring of the EHT sparse measurements (e.g. the hole in the '0' center). Nevertheless, with ngEHT and known rotation axis, many digit features are accurately recovered. For example, note the recovery of the digit '2' (Fig. S1, rows 4–6) which flares up behind the black hole and is distorted by the gravity field.

S3. Static Background Emission

In Sec. 4, the emission was described solely in terms of dynamic sources (e.g., hot-spots) that flare during the observation period and are sheared by the velocity field. In addition to these highly dynamic sources, an *accretion disk* of hot gas rotating around the black hole contributes to the overall lensed emission. Although this accretion disk is also evolving over time, unlike dynamic hot-spots, it can be mostly described by a stationary distribution [2]. Therefore, in this section, show simulation results with the simplification that the accretion disk can be modeled as a known static background emission.

Following Broderick *et al*. [2], we model a static background emission using a *Radiatively Inefficient Accretion Flow* (RIAF) model that is a function of the mass M and spin a of the black hole. The RIAF models the average time-varying emission due to the accretion disk as a 2D static image.Thus, the measurement model of Eq. (6) (and subsequently Eq. 9) can be updated to account for the static background emission

$$\mathbf{y}(t) = \mathbf{F}_t \left[\mathbf{I}(t) + \mathrm{RIAF}(M, a)\right] + \boldsymbol{\varepsilon}. \tag{S13}$$

Figure S2 shows the effect of the RIAF background on the image plane projections. Since we assume that the black hole's mass, M, and spin, a, is known, the RIAF background image is fully defined and Eq. S13 reduces to Eq. (6). In future work, this static background emission could be solved for jointly with the dynamic emission.

In Fig. S3 we show recovery results from the full measurement model, including the static RIAF background, described by Eq. (S13). We demonstrate recoveries for the two emission patterns shown in Sec. 5 of the main text.

The first experiment (top two rows of Fig. S3) has three hot-spots with two "hidden" behind the black hole and one directly visible in-front of the black hole. The image plane, where rays are traced from, is highlighted by a green square. The second experiment has five hot-spots, of which two flare up in front and three flare up behind the black hole. For each experiment we show the recovered volume, e_0 (with PSNR under each reconstruction) and the recovered axis (with the dot product of the recovered and true axis specified under each reconstruction). Furthermore, the image plane and recovery results are shown at t=10 min, with the estimated axis, $\hat{\boldsymbol{\xi}}$, used to propagate time.

S4. Effect of Gravitational Lensing

At first glance it is tempting to say that the effect of gravitational lensing helps the 3D reconstruction by "seeing" behind the black hole. This, however, is not what we observe in simulations. A possible explanation is that the curved rays give rise to a very non-uniform projection condensing much of the 3D space in to a small amount of pixels. Figure S4 shows the image plane over time with and without gravitational lensing. We preform three simulation recoveries:

1. Measurements are synthetsized with lensing and recovery assumes lensing: GR / GR in Fig. S4
2. Measurements are synthetsized with lensing and recovery assumes straight rays: GR / No GR in Fig. S4
3. Measurements are synthetsized with straight rays and recovery assumes straight rays: No GR / No GR in Fig. S4

The recovery results in Fig. S4 (bottom) illustrate the importance of modeling the gravitational lensing effect - neglecting it results in a poor recovery (GR / No GR column). Furthermore the comparison of the GR / GR to No GR/ No GR recoveries highlights the fact that lensing effect does not help to recover the 3D emission field. Rather the 3D recovery relies on the temporal measurements and orbital dynamics model.

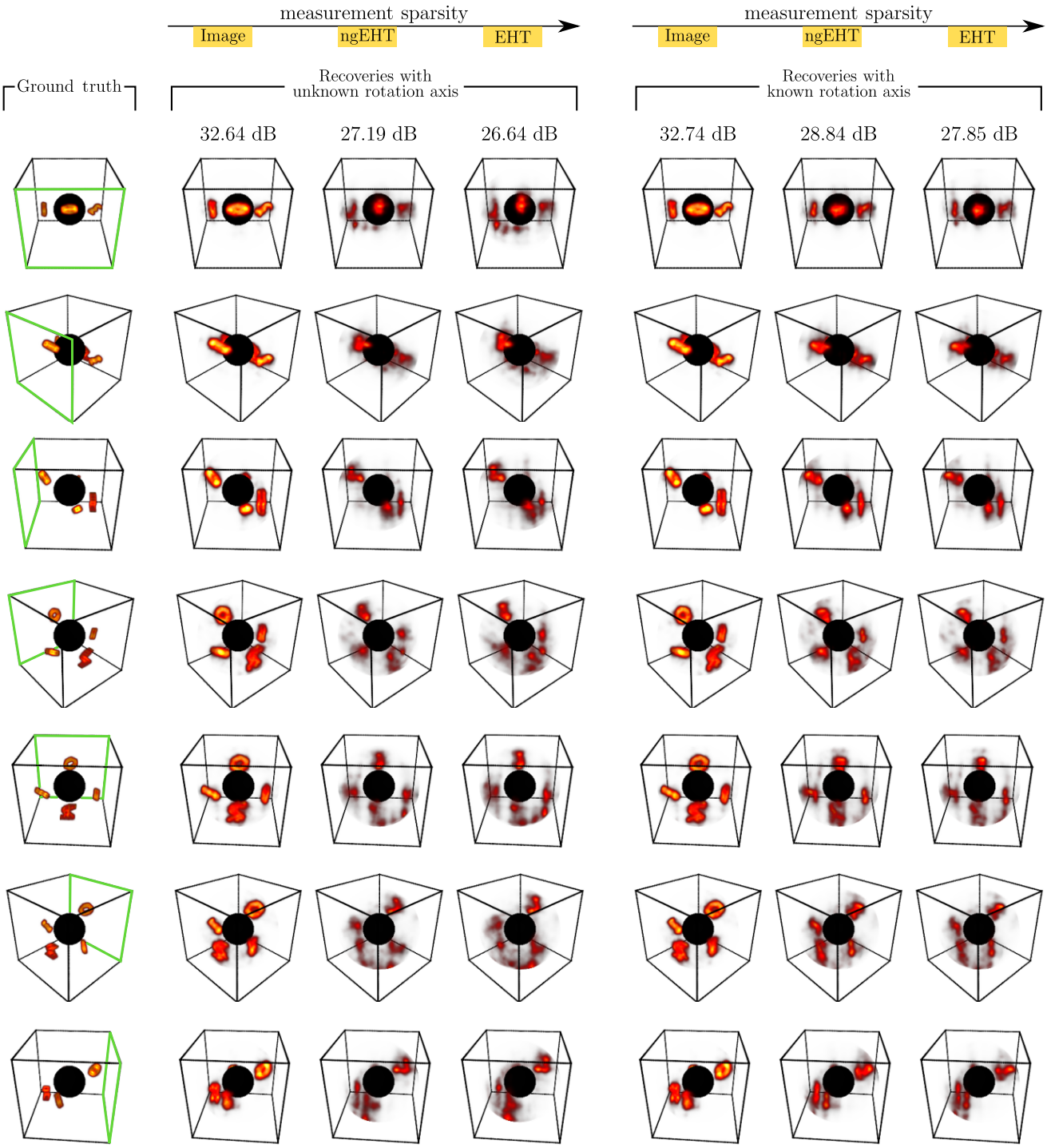

Figure S1. Recovering 3D digits in orbit with known and unknown (estimated) rotation axis. This figure shows the recovery of $e_0(\mathbf{x})$ for different measurement models (full image, ngEHT, EHT). Different rows show the volumes from different directions, where the observation direction is indicated by the green square.

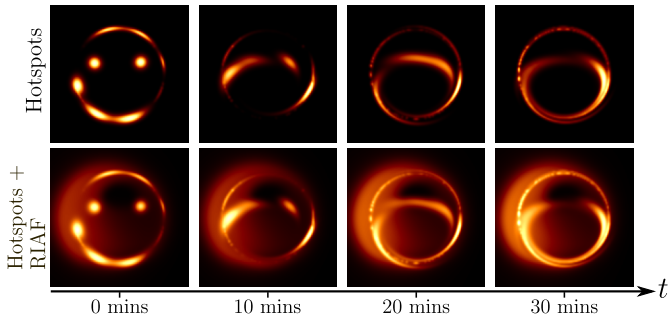

Figure S2. Illustration of the 2D dynamics projected onto the image-plane by integrating along curved rays. The top row shows the dynamic signal produced by the motion of hot-spots with a period of ~ 40 minutes. The bottom row shows the dynamic signal super-imposed on a static background emission modeled, as a radiatively inefficient accretion flow (RIAF) [2].

S5. Initialization and Convergence

Figure S5 illustrates the intialization and convergence of the neural network parameters which dictate the emission field. The estimated emission field is shown at different iterations for three measurement models: Image, ngEHT, EHT. The network is initialized with weights sampled from a Gaussian distribution and the final layer's bias is set to -10 to initialize the emission close to zero. Emission is constrained to be positive by applying a Sigmoid activation to the final layer. The sphere shown in iteration zero illustrates the fact that we recover emission within spherical domain.

S6. Positional Encoding Degree

In our simulations we used a maximum positional encoding degree of $L = 3$. A low degree of L is suitable for volumetric emission fields which are naturally smooth. Figure S6 shows recovery results for different L values. A low value of L acts a s a form of regularization and results in a smoothly varying reconstruction. High L values introduce spurious high frequencies in the recovered emission field.

S7. Telescope Sites

Table 1 contains a list of telescope sites used for EHT and ngEHT simulations (Sec. 5).

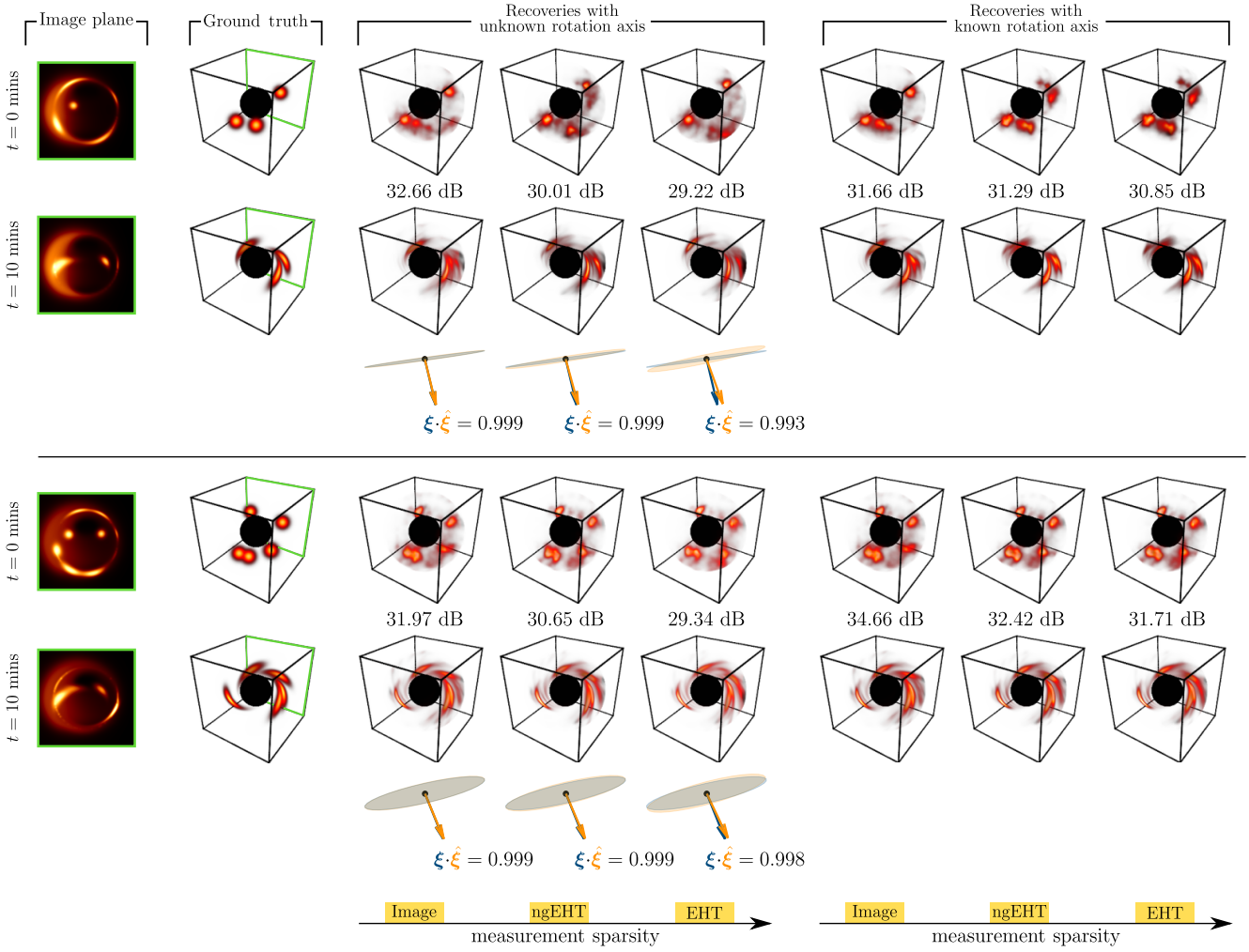

Figure S3. Simulation results for two experiments with different rotation axes and emission patterns. Each experiment shows: the image-plane projection, ground-truth and recoveries at two different times. The orbital period of both is ∼40 minutes. Green highlights the image-plane where rays are traced from. Recoveries are shown for both unknown (estimated) and known rotation axis. At $t = 0$, both experiments have less directly visible hot-spots than hot-spots that are "hidden" behind the black-hole and are lensed onto the image-plane. Quantitative PSNR values for each recovered emission compared to the ground truth are given below each recovery. For the rotation axis the dot product with the ground truth is indicated below each recovery. Images and volumes are shown at $t = 0$ and $t = 10$ minutes.

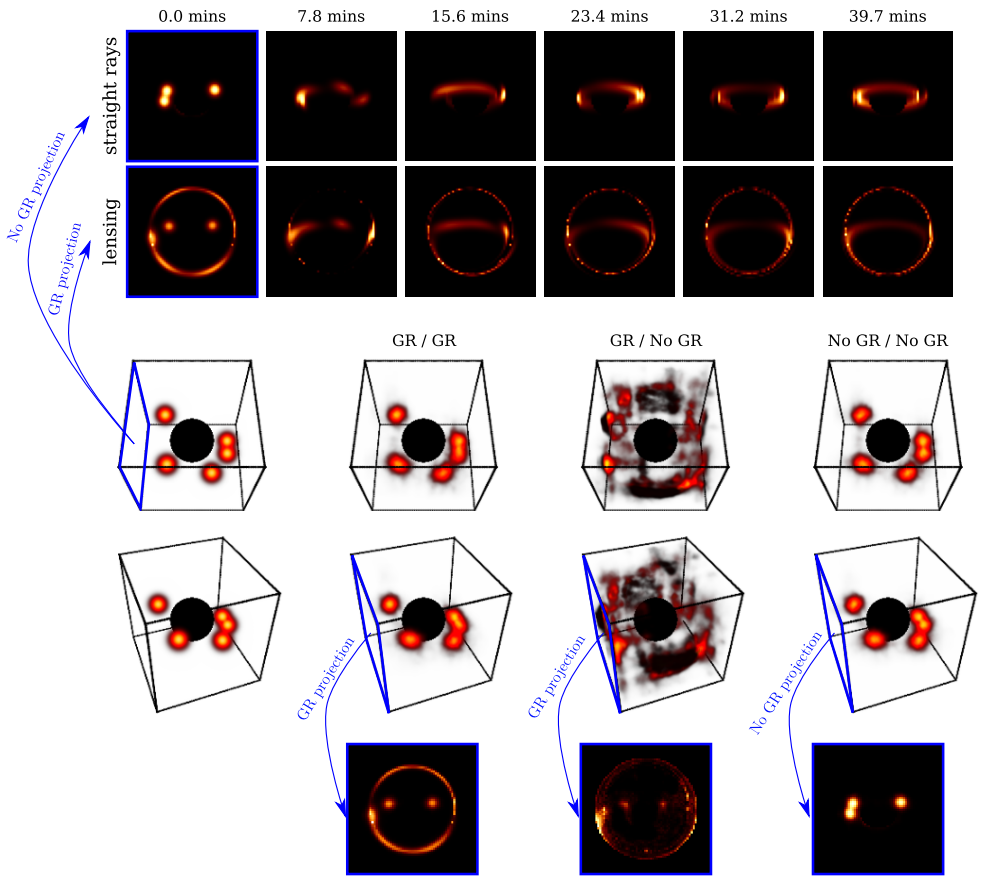

Figure S4. [Top] Image plane with/without gravitational lensing (curved/straight ray projection). [Middle] Recoveries and ground-truth under the different measurement/recovery assumptions specified in Sec. S4. The (GR / No GR) recovery illustrates the importance of modeling the gravitational lensing effect - neglecting it results in a poor recovery. The comparison of (GR / GR) to (No GR/ No GR) highlights that lensing does not help to recover the 3D emission field. Rather, the ability to recover 3D from a single view relies on temporal measurements and an orbital dynamics model. [Bottom] Projection of the recovery using the measurement model (GR / No GR)

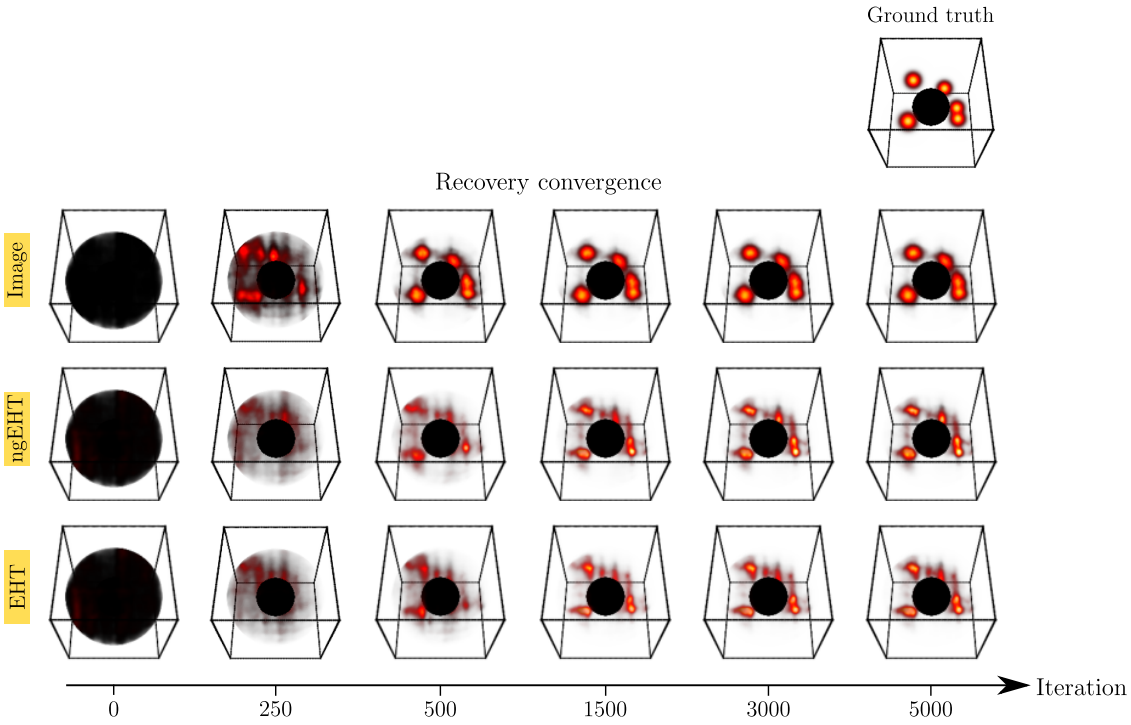

Figure S5. Convergence as a function of iterations for three different measurement models: Image, ngEHT, EHT. The network weights are initialized as samples from a Gaussian distribution and the final layer's bias is set to -10 to initialize the emission close to zero. The sphere shown in iteration zero illustrates the fact that we recover emission within spherical domain. Simulations were run over 5K iterations.

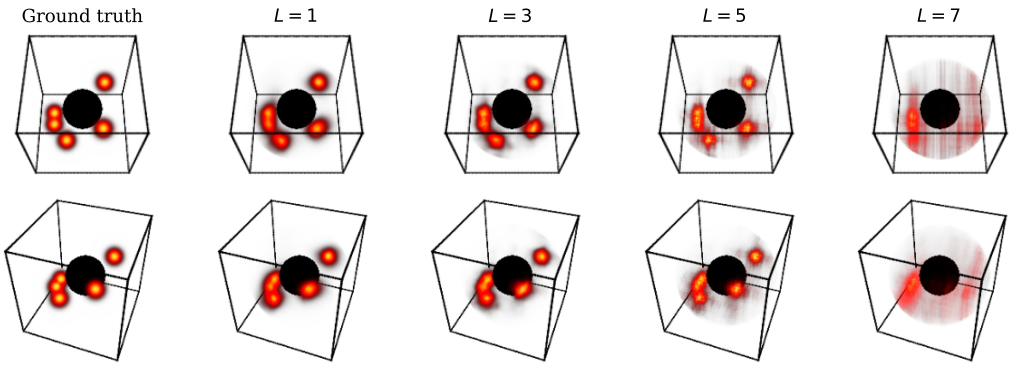

Figure S6. Recovery as a function of maximum positional encoding degree L. A low degree of L acts a s a form of regularization and is suitable for recovery of volumetric emission fields which are naturally smooth. High L introduce spurious high frequencies in the recovery.

Telescopes Sites				
Arrays	Site	Lat. (°)	Lon. (°)	Alt. (m)
EHT	ALMA	-23.03	-67.75	5070
ngEHT	APEX	-23.01	-67.76	5100
	PV	37.07	-3.39	2920
	JCMT	19.82	-155.48	4120
	LMT	18.98	-97.31	4600
	SMA	19.82	-155.48	4110
	SMT	32.70	-109.89	3160
	SPT	-90.00	45.00	2820
ngEHT	BAJA	31	-115	2500
	HAY	43	-71	0
	PIKES	39	-105	4000
	KP	31.57	-111.36	1900
	GAM	23.23	16.1	2300
	GLT	72.3	-38.3	3200
	BAR	38	-118	2250
	CAT	-41	-71	2000
	CNI	29	-18	2000
	GARS	-63	-58	0
	NZ	-44	171	2000
	OVRO	37	-118	1000
	SGO	-33	-70	3500
	CAS	-55	-68	500
	LLA	-24	-66	4500

Table 1. Existing and candidate sites for EHT and ngEHT array.

References

[1] J. M. Bardeen. Timelike and null geodesics in the Kerr metric. In *Black Holes (Les Astres Occlus)*, pages 215–239, Jan. 1973. 2

[2] Avery E. Broderick, Vincent L. Fish, Michael D. Johnson, Katherine Rosenfeld, Carlos Wang, Sheperd S. Doeleman, Kazunori Akiyama, Tim Johannsen, and Alan L. Roy. Modeling seven years of event horizon telescope observations with radiatively inefficient accretion flow models. *The Astrophysical Journal*, 2016. 3, 5

[3] Sean M. Carroll. *Spacetime and geometry. An introduction to general relativity*. 2004. 2

[4] David de la Iglesia Castro. 3D MNIST: A 3D version of the MNIST database of handwritten digits. https://www.kaggle.com/daavoo/3d-mnist. 3

[5] Jason Dexter and Eric Agol. A Fast New Public Code for Computing Photon Orbits in a Kerr Spacetime. *The Astrophysical Journal*, 2009. 2

[6] Samuel E. Gralla and Alexandru Lupsasca. Null geodesics of the Kerr exterior. *Physical Review D*, 2020. 2

[7] M. Mościbrodzka and C. F. Gammie. IPOLE - semi-analytic scheme for relativistic polarized radiative transport. *Monthly Notices of the Royal Astronomical Society*, 2018. 2